

Polarization spectroscopy in rubidium and cesium

M. L. Harris, C. S. Adams, S. L. Cornish, I. C. McLeod, E. Tarleton and I. G. Hughes

Department of Physics, University of Durham, Rochester Building, South Road, Durham DH1 3LE, United Kingdom

(Dated: November 26, 2024)

We develop a theoretical treatment of polarization spectroscopy and use it to make predictions about the general form of polarization spectra in the alkali atoms. Using our model, we generate theoretical spectra for the D2 transitions in ^{87}Rb , ^{85}Rb , and ^{133}Cs . Experiments demonstrate that the model accurately reproduces spectra of transitions from the upper hyperfine level of the ground state only. Among these, the closed transition $F \rightarrow F' = F + 1$ dominates, with a steep gradient through line center ideally suited for use as a reference in laser locking.

PACS numbers: 42.62.Fi, 32.70.Jz, 32.80.Lg 32.30.Jc

I. INTRODUCTION

Polarization spectroscopy is a sub-Doppler spectroscopic technique in which birefringence is induced in a medium by a circularly polarized pump beam, and interrogated with a counterpropagating weak probe beam [1, 2, 3]. It is closely related to saturation spectroscopy, and has proved a useful tool in areas as diverse as combustion diagnostics [4], plasma characterization [5], and laser frequency stabilization [6, 7, 8].

In this work we develop a simple theoretical model of polarization spectroscopy based on a calculation of rate equations. Using this model, we generate spectra for the hyperfine transitions of the D2 lines of rubidium and cesium, and show that for transitions from the upper hyperfine level of the ground state ($n^2S_{1/2}(F = \mathcal{I} + 1/2) \rightarrow n^2P_{3/2}(F' = F + 1, F, F - 1$, where \mathcal{I} is the nuclear spin) our model gives good agreement with the observed spectra. For transitions from the lower hyperfine level, the model breaks down, demonstrating that factors not included in the model play a significant role.

The layout of this paper is as follows. In section 2 we derive expressions needed to construct our model, present results for the time-dependence of the population of relevant hyperfine states, and discuss how spectra are produced. Section 3 describes the experimental apparatus used to test the model's predictions in rubidium and cesium, and section 4 contains experimental and theoretical spectra. Section 5 contains a discussion of our results, and in section 6 we draw our conclusions.

II. THEORY

A. Optical Bloch and population change equations

The density matrix is used to calculate the atom-light interaction. Consider a two level atom with ground state a , excited state b , and transition angular frequency ω_0 , interacting with laser light of angular frequency ω_L and detuning $\Delta = \omega_L - \omega_0$. The Optical Bloch equations are [9]

$$\begin{aligned}\dot{\rho}_{bb} &= -i\frac{\Omega_R}{2}(\tilde{\rho}_{ab} - \tilde{\rho}_{ba}) - \Gamma\rho_{bb} \\ \dot{\tilde{\rho}}_{ba} &= i\Delta\tilde{\rho}_{ba} + i\frac{\Omega_R}{2}(\rho_{bb} - \rho_{aa}) - \frac{\Gamma}{2}\tilde{\rho}_{ba} \\ \dot{\tilde{\rho}}_{ab} &= -i\Delta\tilde{\rho}_{ab} - i\frac{\Omega_R}{2}(\rho_{bb} - \rho_{aa}) - \frac{\Gamma}{2}\tilde{\rho}_{ab} \\ \dot{\rho}_{aa} &= i\frac{\Omega_R}{2}(\tilde{\rho}_{ab} - \tilde{\rho}_{ba}) + \Gamma\rho_{bb}.\end{aligned}\quad (1)$$

Here ρ_{aa} and ρ_{bb} are the ground and excited state probabilities, respectively, and the off-diagonal terms $\tilde{\rho}_{ab}$ and $\tilde{\rho}_{ba}$ are coherences. (The tilde notation means that we are using "slow" variables - i.e. the evolution of the coherence at the laser frequency has been factored out separately). The Rabi frequency is denoted by Ω_R and is proportional to the product of the electric field of the laser and the transition matrix element. The effect of spontaneous emission is to reduce the excited state population at a rate $\Gamma = 1/\tau$, and the coherences at a rate $\Gamma/2$, where τ is the excited state lifetime [9]. There are no collisional terms as the mean time between collisions in the room temperature vapor cells used in these experiments is far longer than the mean time spent in the laser beams. Similar equations are derived for many-level atoms for every Zeeman sub-state.

It becomes much easier to solve these equations if the coherences can be eliminated. To show that such an elimination is valid for our system, we numerically solved the optical Bloch equations containing the coherences and the rate equations for a few sample systems. For a short time the solutions differ; the rate equations are linear in time whereas the optical Bloch equations give a quadratic time dependence for the evolution of populations. However, the solutions become indistinguishable after a time of $\sim 7\tau$ [10], where $\tau=26.24(4)$ ns for rubidium [11] and $30.57(7)$ ns for cesium [12]. As the typical time of flight of an atom through the laser beams (discussed below) is roughly two orders of magnitude longer ($\simeq 5 \times 10^{-6}$ s) it is an excellent approximation to solve the equations for the rate of change of populations. We therefore assume that the coherences evolve sufficiently quickly that their steady state value can be used.

With the coherences eliminated, we set the time derivatives to zero in the second and third equations of (1) and substitute into the first equation, obtaining

$$\begin{aligned}\dot{\rho}_{bb} &= -\frac{\Omega_R^2}{\Gamma} \frac{(\rho_{bb} - \rho_{aa})}{1 + 4\Delta^2/\Gamma^2} - \Gamma\rho_{bb} \\ &= -\frac{\Gamma}{2} \frac{I}{I_{\text{sat}}} \frac{(\rho_{bb} - \rho_{aa})}{1 + 4\Delta^2/\Gamma^2} - \Gamma\rho_{bb}.\end{aligned}\quad (2)$$

This leaves rate equations for populations only. Recalling that the light intensity I is proportional to the square of the Rabi frequency, the saturation intensity I_{sat} is defined as $I/I_{\text{sat}} = 2\Omega_R^2/\Gamma^2$. The three terms on the right-hand side of (2) have the usual physical interpretation: the first represents stimulated emission out of the excited state, which is proportional to the light intensity; the second absorption into the excited state, also proportional to the light intensity; and the third spontaneous emission out of the excited state, which is independent of the light intensity. The intensity-dependent terms have a Lorentzian line-shape, with full width at half maximum of Γ . Note that the usual rate equations of laser physics for populations with Einstein A and B coefficients assume broad-band radiation, and use the intensity per bandwidth (evaluated at line center); in contrast, equation (2) is valid for narrow-band radiation and is a function of the detuning.

It is straightforward to generalize these equations for multilevel systems. As there are three possible polarizations, and the $\Delta F = 0, \pm 1$ selection rule applies, each excited state can decay into up to nine different ground states. The pump beam drives σ^+ transitions, and the Rabi frequencies and saturation intensities are calculated from the known line-strength coefficients.

The line strength for a transition between two states a and b is proportional to the square of the dipole matrix element, given [13] by

$$\begin{aligned}|d_{ab}|^2 &= |e\langle n_b L_b || r || n_a L_a \rangle|^2 \\ &\times (2J_b + 1)(2J_a + 1)(2F_b + 1)(2F_a + 1) \\ &\times \left[\left\{ \begin{matrix} L_b & J_b & S \\ J_a & L_a & 1 \end{matrix} \right\} \left\{ \begin{matrix} J_b & F_b & \mathcal{I} \\ F_a & J_a & 1 \end{matrix} \right\} \left(\begin{matrix} F_a & 1 & F_b \\ m_{F_a} & q & -m_{F_b} \end{matrix} \right) \right]^2\end{aligned}$$

where L and S are respectively the orbital and spin angular momenta of the electron, J is their sum, $F = \mathcal{I} + J$ where \mathcal{I} is the nuclear spin, and m_F is the projection of F onto the z axis. The expressions in curly brackets are standard $6J$ symbols encountered when re-coupling angular momenta, and the term with large round brackets is a $3J$ symbol. These can be calculated using standard symbolic mathematical packages [14]. The value of q denotes the change in z -component of the angular momentum in the transition between the two levels, with $q = 0$ for π transitions, and $q = \pm 1$ for σ^\pm transitions.

As an example, consider ^{87}Rb ($\mathcal{I} = 3/2$), which has two hyperfine states in the ground term, $F = 2, 1$. If the pump laser is tuned in the vicinity of the resonances $S_{1/2}(F = 2) \rightarrow P_{3/2}(F' = 3, 2, 1)$ with the detuning, Δ , defined relative to the closed transition $S_{1/2}(F = 2) \rightarrow P_{3/2}(F' = 3)$, the strongest transition will be $^2S_{1/2}(F = 2, m_F = 2) \rightarrow ^2P_{3/2}(F' = 3, m_{F'} = 3)$. For this transition, the saturation intensity I_{sat} has the value 1.6 mW/cm^2 . The reduced

matrix element for the transition $\langle 5S || r || 5P \rangle = 5.14a_0$, where a_0 is the Bohr radius, is calculated from the excited state lifetime. The line-strength ratios, which we define as

$$R_{F, m_F \rightarrow F', m_{F'}} = \left(\frac{d_{F, m_F \rightarrow F', m_{F'}}}{d_{2, 2 \rightarrow 3, 3}} \right)^2, \quad (4)$$

are always less than one as they are normalized relative to the strongest transition.

To simplify our notation we write the population of a state as P_{F, m_F} , which is equal to the diagonal density-matrix element ρ_{F, m_F, F, m_F} . The five $F = 2, m_F$ ground states obey the rate equations

$$\begin{aligned}\frac{dP_{F, m_F}}{dt} &= - \sum_{F'=F-1}^{F'=F+1} R_{F, m_F \rightarrow F', m_{F'+1}} \frac{\Gamma}{2} \frac{I}{I_{\text{sat}}} \frac{(P_{F, m_F} - P_{F', m_{F'+1}})}{1 + 4(\Delta'/\Gamma)^2} \\ &+ \sum_{m_{F'}=m_F-1}^{m_{F'}=m_F+1} \sum_{F'=F-1}^{F'=F+1} R_{F, m_F \rightarrow F', m_{F'}} \Gamma P_{F', m_{F'}},\end{aligned}\quad (5)$$

where $\Delta' = \Delta$ if $F' = F + 1$; $\Delta' = \Delta + \Delta_{32}$ if $F' = F$; and $\Delta' = \Delta + \Delta_{31}$ if $F' = F - 1$. Here $\hbar\Delta_{32}$ and $\hbar\Delta_{31}$ are the excited state hyperfine intervals. The first row of Eq. (5) contains the stimulated absorption and emission terms, the second row the spontaneous emission terms.

The three $F = 1, m_F$ ground states obey the rate equations

$$\frac{dP_{F, m_F}}{dt} = \sum_{m_{F'}=m_F-1}^{m_{F'}=m_F+1} \sum_{F'=F-1}^{F'=F+1} R_{F, m_F \rightarrow F', m_{F'}} \Gamma P_{F', m_{F'}}.\quad (6)$$

Note that there are no stimulated terms as the large ground state splitting means that these transitions very far off resonance; these states can only increase their population by spontaneous emission from the excited states.

Finally, the excited state population rate equations are

$$\begin{aligned}\frac{dP_{F', m_{F'}}}{dt} &= \sum_{F=2} R_{F, m_{F'}-1 \rightarrow F', m_{F'}} \frac{\Gamma}{2} \frac{I}{I_{\text{sat}}} \frac{(P_{F, m_{F'}-1} - P_{F', m_{F'}})}{1 + 4(\Delta'/\Gamma)^2} \\ &- \sum_{m_F=m_{F'}-1}^{m_F=m_{F'}+1} \sum_{F=F'+1} R_{F, m_F \rightarrow F', m_{F'}} \Gamma P_{F', m_{F'}}.\end{aligned}\quad (7)$$

A useful check before solving these equations is that the sum of all of the right-hand sides of these equations must be zero, because the total population in all states is constant. Note that there are 36, 24, or 48 Zeeman levels which have to be considered for the ^{85}Rb , ^{87}Rb , and ^{133}Cs systems, respectively; hence the simplification of the equations by eliminating the coherences is substantial.

B. Calculation of anisotropy

The birefringence of the medium can be probed by a linearly polarized probe beam, which can be decomposed into two beams of equal amplitude and opposite circular polarization. For an isotropic medium, both circular components experience the same refractive index and absorption. There is a difference in absorption coefficients, $\Delta\alpha$, for an optically pumped medium: $\Delta\alpha = \alpha_+ - \alpha_-$, with α_{\pm} being the absorption coefficients of the circular components driving σ^{\pm} transitions. Correspondingly, the incident linearly polarized beam exits the medium with a rotated elliptical polarization. Both the ellipticity and the angle of rotation are proportional to $\Delta\alpha$ [6]. In our experimental set-up (Section 3) we are sensitive to the rotation of polarization, providing the absorption coefficients are not too large. The signal has a characteristic dispersion spectrum (equation (9) in [6]). Therefore for each resonance we calculate one parameter, the line-center difference in absorption.

The experiments were performed with alkali metal atoms (^{85}Rb , ^{87}Rb , ^{133}Cs) on the D2 transition. For an atom in the $^2S_{1/2}$ ground state with nuclear spin \mathcal{I} there are two values for the total angular momentum F , namely $F = \mathcal{I} \pm 1/2$. There are four values for the excited state angular momentum F' , namely $F' = \mathcal{I} \pm 3/2, \mathcal{I} \pm 1/2$. The hyperfine splitting of the ground states (3.0 GHz for ^{85}Rb , 6.8 GHz for ^{87}Rb , 9.2 GHz for ^{133}Cs) exceeds the room temperature Doppler width (~ 0.5 GHz), whereas the excited state hyperfine splitting is less than the Doppler width. Therefore, the absorption spectrum consists of two isolated Doppler broadened absorption lines per isotope. Sub-Doppler absorption features are obtained by using counter-propagating pump and probe beams. There are three excited state resonances coupled to each ground state via electric dipole transitions, namely $S_{1/2}(F) \rightarrow P_{3/2}(F' = F + 1, F, F - 1)$. In addition, one observes three cross-over resonances at frequencies halfway between each pair of conventional resonances [15].

The calculation assumes that there is no excited state population initially, and that the ground state population is spread uniformly amongst the $2(2\mathcal{I} + 1)$ different $|F, m_F\rangle$ levels. The pump beam has intensity I and drives σ^+ transitions. This optical pumping process drives the population towards the largest possible value of m_F , and the medium becomes optically anisotropic. Equations similar to (2) are written down for each m_F level, and the set of coupled equations are solved numerically.

From these solutions, we obtain graphs of the population of each hyperfine state as a function of time. Figure 1 shows the time-evolution of these populations for a sample of ^{87}Rb atoms when $\Delta/2\pi = 0, -267$ MHz, and -424 MHz, corresponding to a laser on resonance with the $F = 2 \rightarrow F' = 3, 2, 1$ transitions respectively. When the laser is resonant with the closed $F = 2 \rightarrow F' = 3$ transition, atoms are rapidly pumped into the extreme $|2, 2\rangle$ state, with over 50% of atoms in this state after $< 10 \mu\text{s}$. The population of the other states is either constant or decreasing after $\sim 1 \mu\text{s}$.

These figures clearly show the different optical pumping dynamics as a function of the laser detuning. A detuning

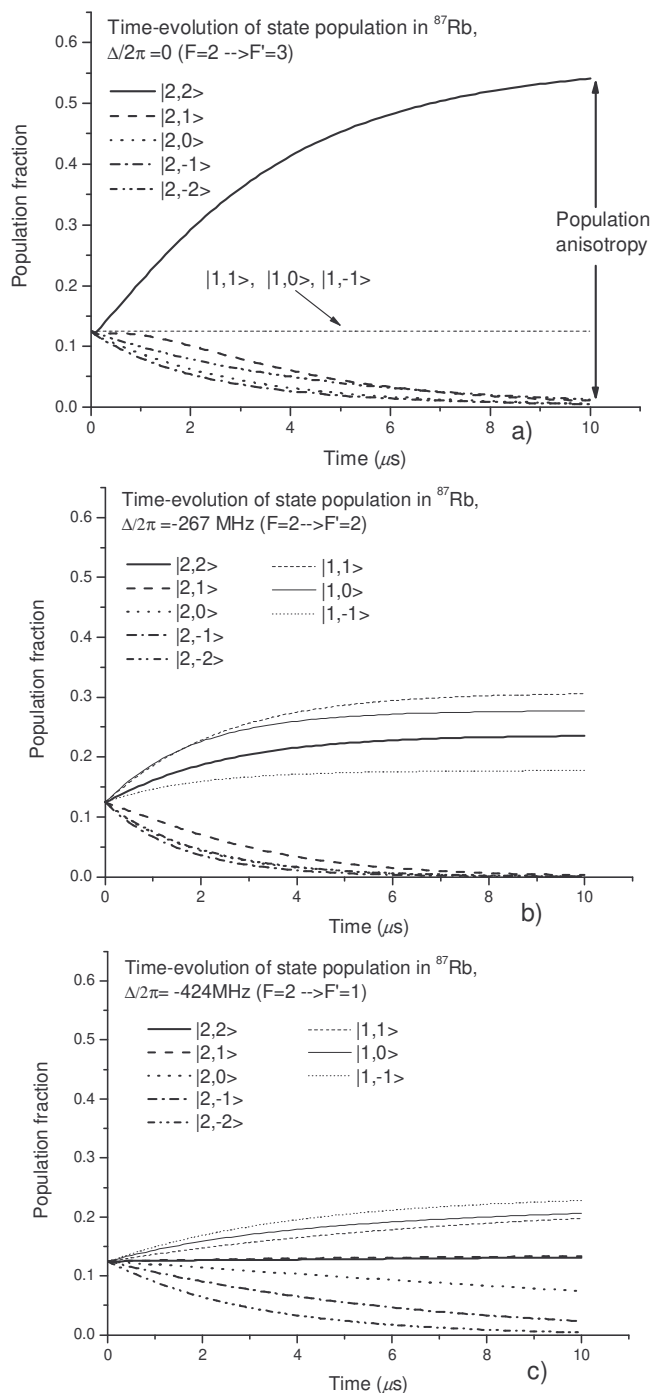


FIG. 1: Time-evolution of population. The population of the eight ground state sub-levels of ^{87}Rb are plotted as a function of time after the pump beam is turned on. The pump drives σ^+ transitions and has an intensity of $0.1I_{\text{sat}}$. Vertical axes are identical to emphasize differences in population behavior. a) Laser tuned to $F = 2 \rightarrow F' = 3$ transition. Within a few μs the initial isotropic population distribution becomes highly anisotropic, as atoms are optically pumped into the $|2, 2\rangle$ state. As this transition is closed, no change occurs in the population of the $F = 1$ manifold. b) When the laser is tuned to the $F = 2 \rightarrow F' = 2$ transition the atoms are again optically pumped towards the $|2, 2\rangle$ state. However, as this is an open transition, a significant fraction of population accumulates in the $F = 1$ manifold. These states do not contribute to the medium's optical anisotropy. c) For the laser turned to the $F = 2 \rightarrow F' = 1$ transition even fewer atoms are pumped into the $|2, 2\rangle$ state.

$\Delta=0$ (Figure 1a) is optimum for achieving the most optically anisotropic medium. For $\Delta/2\pi=-267$ MHz (Figure 1b) the medium becomes optically anisotropic, but to a lesser extent. This is due to the open nature of the transition, which allows atoms to accumulate in the $F = 1$ manifold, where they are too far from resonance to influence the medium's anisotropy. This effect is even more pronounced for $\Delta/2\pi=-424$ MHz (Figure 1c), and the medium's optical anisotropy at this detuning is correspondingly reduced in comparison with the other detunings.

These population graphs allow us to predict that the polarization spectroscopy signal should be dominated by the closed transitions, $S_{1/2}(F = \mathcal{I} + 1/2) \rightarrow P_{3/2}(F' = F + 1)$ and $S_{1/2}(F = \mathcal{I} - 1/2) \rightarrow P_{3/2}(F' = F - 1)$. For such transitions, selection rules forbid atoms in the excited state from falling into the other ground state; consequently, all of the ground state population ends up pumped into the extreme magnetic sublevels with $m_F = F$ (for $\mathcal{I} + 1/2$, as discussed in the example above) or $m_F = F$ and $m_F = F - 1$ (for $\mathcal{I} - 1/2$). The absorption coefficients α_{\pm} differ most for this extreme state; therefore, the anisotropy of the medium is maximized. Note that the sign of the anisotropy generated by the $\mathcal{I} + 1/2$ transitions is expected to be opposite that of the lower hyperfine transitions, due to the lack of allowed σ^+ transitions from the ground $m_F = F = \mathcal{I} - 1/2$ states. Figure 2 illustrates the optical pumping process.

After solving the coupled population rate equations it is possible to calculate the time-dependent anisotropy of the medium, $\mathcal{A}(t)$. This is defined as a sum over all of the ground m_F states of the difference in the absorption coefficients for the components of the probe beam driving σ^{\pm} transitions, taking into account the ground and excited state populations:

$$\mathcal{A}(t) = \sum_{m_F=-F}^{m_F=+F} \alpha_{(F,m_F \rightarrow F',m_{F+1})} (P_{F,m_F} - P'_{F',m_{F+1}}) - \alpha_{(F,m_F \rightarrow F',m_{F-1})} (P_{F,m_F} - P'_{F',m_{F-1}}). \quad (8)$$

For each isotope and each ground state F the anisotropy is calculated for the three frequencies corresponding to the resonances $F \rightarrow (F' = F + 1, F, F - 1)$, i.e. $\Delta=0, -\Delta_{32}$, and $-\Delta_{31}$. It is assumed that since the experiment uses counter propagating pump and probe beams only atoms with zero velocity along the axis of the beams contribute significantly. The details of the transverse motion of the atoms is outlined in the next sub-section.

C. Transverse motion of atoms

The experiment measures the average anisotropy of the medium. To simulate this, we average the time-dependent anisotropy, $\mathcal{A}(t)$, with a weighting function, $\mathcal{H}(t)$, which gives the distribution of times of flight transverse to the beam. For a circular beam of radius a the probability distribution,

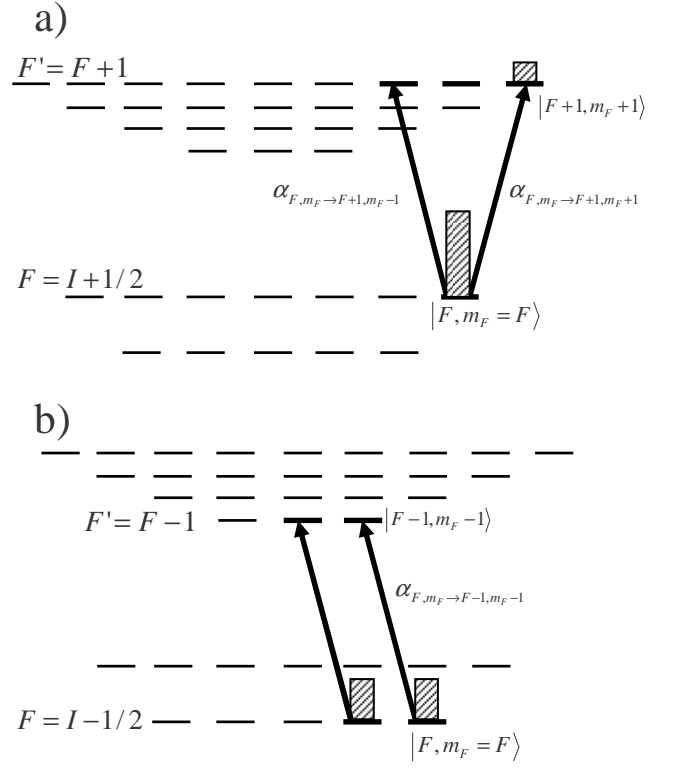


FIG. 2: Sign of anisotropy for closed transitions. a) For the closed $F = \mathcal{I} + 1/2 \rightarrow F' = F + 1$ transition the population is optically pumped into the $|F, m_F = F\rangle$ state, with a small fraction in the excited state. The line strength $\alpha_{F, m_F \rightarrow F+1, m_{F+1}}$ is significantly larger than $\alpha_{F, m_F \rightarrow F+1, m_{F+1}-1}$. b) For the closed $F = \mathcal{I} - 1/2 \rightarrow F' = F - 1$ transition the population is optically pumped into the $|F, m_F = F\rangle$ and $|F, m_F = F - 1\rangle$ states. There are no allowed σ^+ transitions for these states, whereas the line strength for the σ^- transitions are finite. Consequently, the anisotropy of the medium has opposite sign relative to a). All levels are drawn as for an atom with $\mathcal{I} = 5/2$; the structure of the other alkali atoms is similar.

$\mathcal{F}(\ell)$, of having a path length ℓ in a uniform gas is

$$\mathcal{F}(\ell) = \frac{\ell}{2a\sqrt{4a^2 - \ell^2}}. \quad (9)$$

The probability distribution function, $\mathcal{G}(t, \ell)$, for having a transit time t for a given ℓ is obtained from the Maxwell velocity distribution for a sample of atoms of mass m at temperature T and is

$$\mathcal{G}(t, \ell) = \frac{m\ell^2}{k_B T^3} \exp\left(-\frac{m\ell^2}{2k_B T t^2}\right). \quad (10)$$

The distribution function $\mathcal{H}(t)$ is obtained thus:

$$\mathcal{H}(t) = \int_{\ell=0}^{2a} \mathcal{G}(t, \ell) \mathcal{F}(\ell) d\ell, \quad (11)$$

which can either be evaluated numerically or in closed form in terms of the complex error function. The average anisotropy $\bar{\mathcal{A}}$ is calculated by averaging the time-dependent anisotropy

with the time of flight weighting function, i.e.:

$$\bar{A} = \int A(t)\mathcal{H}(t)dt. \quad (12)$$

This integral is calculated numerically at the three resonant frequencies of each D2 transition.

D. Generating theoretical spectra

To generate the predicted spectra, the three values of \bar{A} from (12) are multiplied by dispersion functions of the form $x/(1+x^2)$, where $x = 2\Delta/\Gamma$. As in the work of Yoshikawa *et al.* [16] the strength of cross-over features is assumed to be the average of the two associated resonances; hence cross-over features are calculated by multiplying this average by a dispersion function located halfway between each resonance.

To account for spectral broadening produced by saturation effects (power broadening), we substituted a broadened linewidth $\gamma = k\Gamma$ MHz for the natural linewidth Γ in the dispersion function. We found that for $1 \leq k \leq 2$, the experimental data do not provide a tight constraint on the value of γ . Doppler broadening is incorporated by convolving the resulting spectra with a Gaussian of FWHM $\leq 1 \times 2\pi$ MHz, consistent with residual Doppler broadening due to the finite crossing angle between the probe and pump beams. Magnitudes for both types of broadening were set by the experimental conditions, as were the values for temperature (293K for rubidium, 273K for cesium), beam radii, and I/I_{sat} .

III. EXPERIMENTAL SETUP

The layout of our experiment is similar to that described in [6] and is shown in Figure 3. The probe beam's plane of polarization is set at $\pi/4$ with respect to a polarizing beam splitter (PBS), which acts as an analyzer. The signal we record is the difference between the signals in each arm of the PBS; in the absence of a pump beam, the two arms will have equal intensities, and the difference will be zero. This technique produces polarization signals an order of magnitude larger than the conventional (single detector) method of polarization spectroscopy - an important advantage if the signal is being used for laser locking [6].

The experimental layouts for rubidium and cesium spectroscopy are very similar, differing only in the length of the alkali vapor cell, equipment used to control the magnetic field along the axis of the cell, and waveplate type. Table 1 contains information on the spot radii ($1/e^2$ intensities) of the beams after the light has passed through a pair of anamorphic prisms.

In both experiments the pump and probe beams are derived from the same extended cavity diode laser (ECDL). The diode for the rubidium (cesium) laser was a Sanyo DL-7140-201 (SDL-5401-G1). The crossing angle between probe and counterpropagating pump within the vapor cell is $<3.0 \pm 0.2$ mrad. Neutral density filters are used to vary pump and probe powers independently. A half-wave plate rotates the polarization of the probe relative to the axis of the PBS; a quarter-wave plate

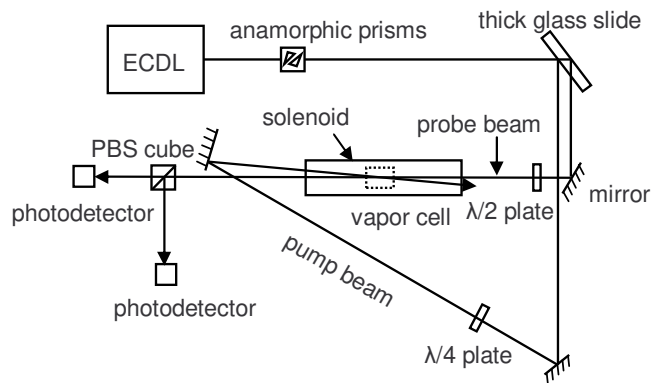


FIG. 3: Experimental layout. A thick glass slide picks off a fraction of the extended cavity diode laser (ECDL) light and splits it into two parallel beams. One beam acts as the probe, and the other as a (nearly) counterpropagating pump. The beams overlap inside a 70 mm (50 mm) Rb (Cs) cell, which rests inside a long solenoid and below a coil that cancels the ambient laboratory field. In the cesium experiment two coils in the Helmholtz configuration replace the solenoid. A half-wave plate rotates the plane of polarization of the probe beam with respect to the polarizing beam splitter (PBS) cube axis; a quarter-wave plate makes the pump circularly polarized.

TABLE I: Specifications of lasers used in this work.

Atom	λ	Horizontal r ($1/e^2$)	Vertical r ($1/e^2$)
Rb	780 nm	0.65 ± 0.01 mm	0.59 ± 0.01 mm
Cs	852 nm	0.69 ± 0.01 mm	0.70 ± 0.01 mm

converts light in the pump beam to circular polarization. The two output beams from the PBS are focused onto photodiodes, which are connected to simple current-to-voltage circuits designed to output a voltage linearly proportional to the incident intensity. These voltages are then subtracted electronically to yield the polarization spectra.

Since light of a given polarization may drive σ^+ , σ^- or π transitions depending on the external magnetic field, it is necessary to establish a “preferred” magnetic field direction along the vapor cell axis. In the rubidium experiment this is done by placing a room-temperature cell containing ^{85}Rb and ^{87}Rb inside a 300-turn solenoid of length 280 mm and diameter 26 mm. Numerical simulations showed that the magnetic field inside the solenoid is uniform to within 0.2% over the length of the 70 mm cell.

In the cesium experiment the cell is partially submerged in an ice bath, and two 300×300 mm square coils in the Helmholtz configuration generate an axial magnetic field uniform to 1%. The ice bath is needed because our model assumes an optically thin medium, but at 23 °C absorption exceeds 90% for a 50 mm Cs vapor cell (compared to a maximum of 30% for Rb in a 70 mm cell). In the ice bath this is reduced to 60% (50%) for transitions from the upper (lower) hyperfine level of the ground state. In both experiments we also cancel the (primarily vertical) ambient laboratory mag-

netic field with a 245 mm diameter coil mounted above the cell. Any inhomogeneity due to the finite diameter of this coil makes a negligible contribution to the total field when added in quadrature with the axial field. The magnitude of the axial field is set to a value just below the point where Zeeman splitting of the hyperfine levels begins to distort the polarization spectra, typically $\simeq 150 \mu\text{T}$.

IV. RESULTS

Figure 4 shows the data obtained with the layout described in the last section (thick line) and the theoretical spectra (thin line). All experimental spectra were taken with pump and probe beam intensities $\leq 0.1 I_{\text{sat}}$ to reduce saturation effects. The spectra shown are of transitions from the upper hyperfine level of the ground state, i.e. the $5^2S_{1/2}$ ($F = 2$) \rightarrow $5^2P_{3/2}$ ($F' = 1, 2, 3$) transitions in ^{87}Rb , $5^2S_{1/2}$ ($F = 3$) \rightarrow $5^2P_{3/2}$ ($F' = 2, 3, 4$) transitions in ^{85}Rb , and $6^2S_{1/2}$ ($F = 4$) \rightarrow $6^2P_{3/2}$ ($F' = 3, 4, 5$) transitions in ^{133}Cs . The closed transitions in this group are the well-known ‘‘cooling’’ transition used in laser-cooling experiments. Zero detuning is relative to the highest-frequency transition, and all detunings are given in units of $\Delta/2\pi$. The magnitude of each feature is given in volts, and will depend on the gain resistance in the photodiode circuit ($1 \text{ M}\Omega$ in our experiment). For Cs, two sets of data are shown; one taken with the vapor cell at room temperature (dashed line), the other with the cell in an ice bath as described in the previous section (solid line).

In these spectra, polarization signals of closed transitions dominate, with magnitudes up to three times that of the next largest feature. This is true for all three species, and is in marked contrast with conventional saturated absorption/hyperfine pumping spectra [17]. As predicted, the $F \rightarrow F' = F$ transitions produce a moderate amount of anisotropy, and the lowest frequency open transitions give the smallest signal. A graph showing the distribution of times of flight for rubidium at room temperature through a beam with the experimental waist shows a most probable time of flight of $5 \mu\text{s}$, and a significant fraction of the atoms with times of flight longer than $10 \mu\text{s}$. Therefore we do indeed see that the timescale needed to build up anisotropy is significantly longer than the spontaneous decay time, and comparable to transit times. The accumulation of anisotropy can be accelerated by using a more intense pump beam; however, this will not greatly increase the signal as most atoms are already pumped into the extreme state within the transit time. This is also what is observed experimentally.

Spectra taken of transitions from the lower hyperfine level of the ground state show a more complicated pattern. The (low-frequency) closed transitions in Cs and ^{85}Rb show a characteristic strong dispersion feature, but in ^{87}Rb the largest feature arises from one of the cross-over peaks (Figure 5). In ^{85}Rb closely-spaced transitions generate a polarization spectrum in which individual peaks merge, making exact matching of features and transitions difficult.

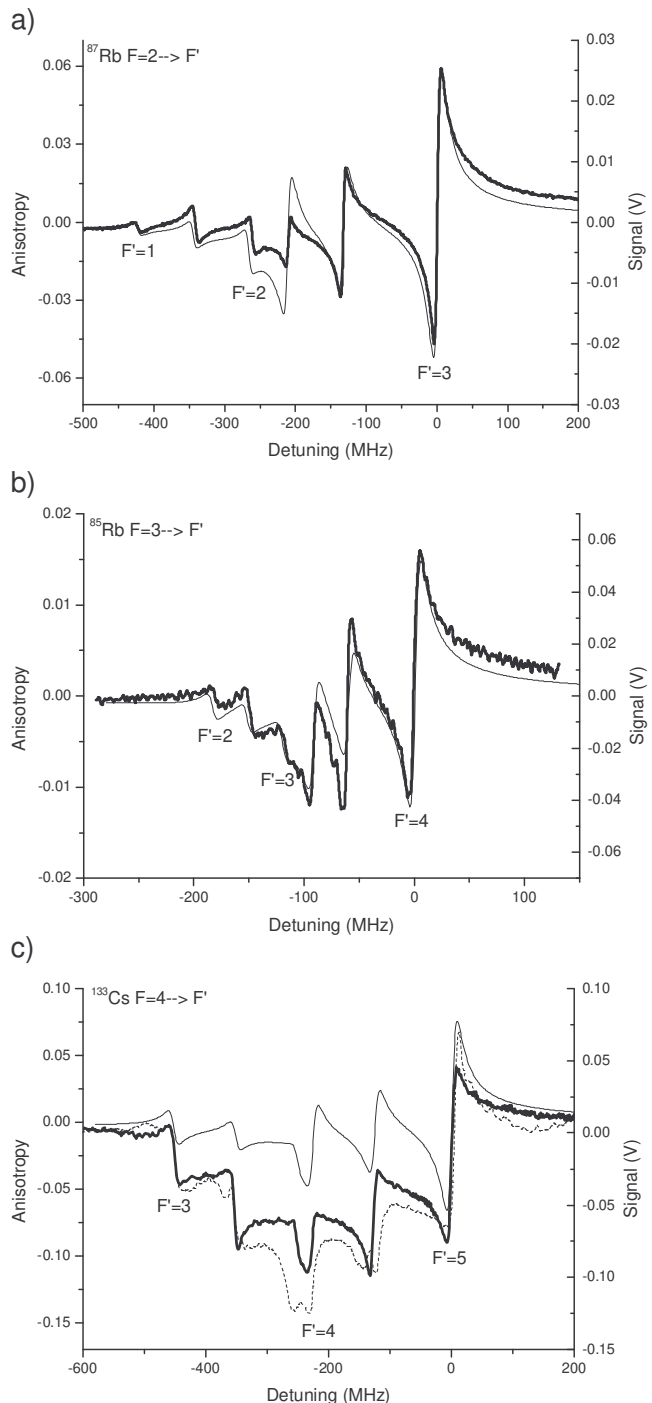


FIG. 4: Experimental (thick line) and theoretical (fine line) polarization spectra of D2 line transitions in a) ^{87}Rb , b) ^{85}Rb , and c) ^{133}Cs . Spectra were obtained by tuning the laser frequency to drive transitions from the upper hyperfine level of the atom’s ground state. All three spectra are dominated by the strong dispersion features associated with the closed transition. For the Cs upper hyperfine spectra, solid (dashed) lines represent spectra taken with the vapor cell at 0° (23°) C.

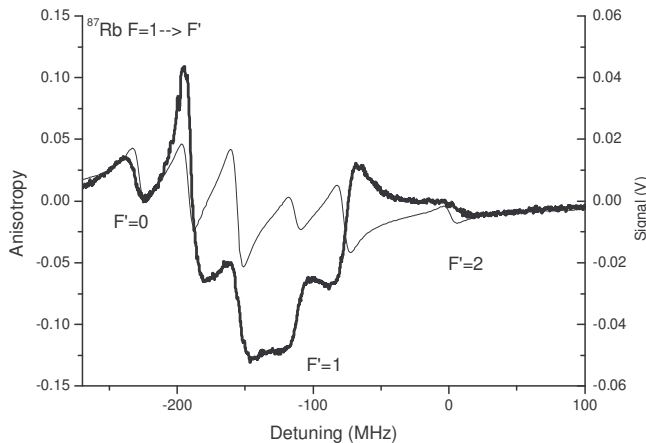


FIG. 5: Experimental (thick line) and theoretical (fine line) polarization spectra of D2 line transitions from the lower hyperfine level of the ground state in ^{87}Rb .

V. DISCUSSION

By comparing theoretical and experimental traces, we see immediately that our model reproduces experimental features of upper hyperfine transition spectra with a high degree of accuracy. Fine spectral details like the “horns” resulting from the closely-spaced $F = 2 \rightarrow F' = 2$ and $X_{3,1}$ cross-over peak in ^{87}Rb arise automatically from the calculated anisotropies. The magnitudes of theoretical spectral peaks relative to the large closed transition peaks also agree well with experimental data, especially in ^{85}Rb . The effect of reducing vapor pressure by cooling the Cs cell is readily apparent. Although the central peaks are still offset from theoretical spectra compared to their counterparts in the Rb spectra, the magnitude of the offset is significantly less at 0 °C than at room temperature, and the shapes of the spectra broadly agree.

For lower hyperfine spectra (e.g. the ^{87}Rb spectra in Figure 5), we observe that the sign of the anisotropy for the closed-transition peak is reversed compared to corresponding peaks in upper hyperfine spectra, as predicted in our model. However, most other spectral features differ markedly from predictions. Crucially, though, the model spectra show similar discrepancies for each of the three species, indicating that the lack of agreement must be due to physical processes not included in our model. As a test, we ran our simulation again, this time allowing the position and magnitude of the three Lorentzians (representing three transitions) to float unconstrained by any input parameters. We found that no values of detuning or anisotropy could account for the observed spectra.

To gain insight into the anisotropies induced by lower hyperfine transitions (particularly “open” transitions, i.e. those with a decay channel to the other ground state level), we performed experiments designed to measure the anisotropy directly. As in Reference [6], a quarter-wave plate was inserted before the PBS, oriented such that it converted the circular polarization component of the probe which drives σ^+ (σ^-) transitions into vertically (horizontally) polarized light. The output from the arms of the PBS then directly measures the

absorption experienced by the components driving σ^+ and σ^- transitions.

For upper hyperfine transitions, the largest anisotropies (i.e. largest difference in signal between the two arms) resulted from the closed transitions. This agrees with theoretical predictions and is reflected in our data. For lower hyperfine transitions, large and strongly negative anisotropies occurred at the cross-over frequencies - a fact reflected in our data, but not in the model. This suggests that for such transitions, it is no longer valid to assume that the strength of crossover features is the average of the two associated resonances.

The present model assumes a uniformly distributed circular laser beam. The experimental beam has a Gaussian profile, which will lead to slight variations in the absolute height of the spectroscopic peaks. It will not, however, account for the difference between upper and lower hyperfine transitions. It is also possible that if the optical pumping is not complete for the lower hyperfine states, ignoring the coherences could have a large effect. The most significant approximation that is likely to break down for lower hyperfine transitions is the assumption that only atoms with no axial velocity will contribute to the anisotropy. As was shown in [17], a full description of the spectrum, especially open transitions, must take into account a large velocity class of atoms moving along the beam, not just the “stationary” ones. The contribution of these nonzero velocity classes will be more significant for $F = \mathcal{I} - 1/2$ because the line strength factors for the closed transition are weakest; for $F = \mathcal{I} + 1/2$, line strength factors are strongest for the closed transition, and the “stationary atom” approximation is reasonable.

Expanding the model to include a large velocity class would be computationally intense, and is beyond the scope of this work. Walewski et al. have performed numerical simulations which included nonzero axial velocities, and successfully used their model to explain features of polarization spectra in flames [18]. However, the organic molecules they studied have very different structures and properties from those of the alkali atoms examined here, and adapting their model to account for alkali spectra would be correspondingly nontrivial.

In comparing theoretical predictions with experimental signals, we have chiefly focused on the shape and relative magnitudes of spectral features. The absolute magnitude of the experimental polarization spectroscopy signal depends not only on the gain resistor in the photodiode circuit, as discussed in the previous section, but also on the intensity of the probe beam in the absence of a vapor cell (see Eq. 7 in reference [6]). This in turn depends on the optical thickness of the vapor, which is both temperature-dependent (as noted earlier in our discussion of cesium) and different for each species. Because of these factors, the species with the largest calculated anisotropy will not necessarily produce the largest experimental signal. Our decision to display theoretical and experimental spectra on separate scales reflects these considerations.

Finally, we note that although the peaks associated with the closed transitions in the upper hyperfine spectra are ideal for laser locking, with steep slopes centered on line center, this is not true for the lower hyperfine spectra, where the position of

each zero crossing is not trivially related to the position of the resonances.

VI. CONCLUSIONS

We have presented a model of polarization spectroscopy based on numerical integration of population rate equations, and shown how this model can be used to simulate the optical pumping process that leads to an anisotropic population distribution, and thus an optically anisotropic medium. Theoretical polarization spectra generated by this model account very well for $F = \mathcal{I} + 1/2 \rightarrow F'$ transitions in ^{87}Rb , ^{85}Rb , and ^{133}Cs , but not as well for $F = \mathcal{I} - 1/2 \rightarrow F'$ transi-

tions. For $F = \mathcal{I} + 1/2 \rightarrow F'$, the closed $F' = F + 1$ transition dominates the spectra, with a steep slope through laser locking. Although we have not studied them experimentally in this work, we would expect similar results for the D2 spectra of other alkali species, e.g. ^6Li and ^{23}Na .

Acknowledgements

We thank V. Jacobs and R. C. Shiell for valuable discussions. We acknowledge support from the UK EPSRC, the Universities UK Overseas Research Scheme (MLH) and the Royal Society (SLC).

-
- [1] C. Wieman and T. W. Hänsch, *Phys. Rev. Lett.* **36**, 1170 (1976).
 - [2] R. E. Teets, F. V. Kowalski, W. T. Hill, N. Carlson, and T. W. Hänsch, *Advances in Laser Spectroscopy* **113**, 80 (1977).
 - [3] W. Demtröder, *Laser Spectroscopy* (Springer, Berlin, 1998).
 - [4] A. C. Eckbreth, *Laser Diagnostics for Combustion Temperature and Species* (Overseas Publishers Association, Amsterdam, 1996).
 - [5] K. Danzmann, K. Grützmacher, and B. Wende, *Phys. Rev. Lett.* **57**, 2151 (1986).
 - [6] C. P. Pearman, C. S. Adams, S. G. Cox, P. F. Griffin, D. A. Smith and I. G. Hughes, *J. Phys. B.* **35**, 5141 (2002).
 - [7] A. Ratnapala, C. J. Vale, A. G. White, M. D. Harvey, N. R. Heckenberg, H. Rubinsztein-Dunlop, *Opt. Lett.* **29**, 2704 (2004).
 - [8] E. W. Streed, A. P. Chikkatur, T. L. Gustavson, M. Boyd, Y. Torii, D. Schneble, G. K. Campbell, D. E. Pritchard, and W. Ketterle, *Rev. Sci. Instrum.* **77**, 023105 (2006).
 - [9] C. Cohen-Tannoudji, *Atom-Photon Interactions* (Wiley, 1992, Chapter V).
 - [10] N. Coppendale, MSci Report, Durham University, unpublished (2005).
 - [11] U. Volz and H. Schmoranzer, *Phys. Scr.*, T **165**, 48 (1996).
 - [12] R. J. Rafac, C. E. Tanner, A. E. Livingston, and H. G. Berry, *Phys. Rev. A* **60**, 3648 (1999).
 - [13] A. R. Edmonds, *Angular Momentum in Quantum Mechanics*, 2nd ed. (Princeton, 1960).
 - [14] We use the software package *Mathematica*, available from Wolfram Research Incorporated.
 - [15] K. B. MacAdam, A. Steinbach, and C. E. Wieman, *Am. J. Phys.* **60**, 1098 (1992).
 - [16] Y. Yoshikawa, T. Umeki, T. Mukae, Y. Torii, T. Kuga, *Applied Optics* **42**, 6645 (2003).
 - [17] D. A. Smith and I. G. Hughes, *Am. J. Phys.* **72**, 631 (2004).
 - [18] J. Walewski, C. F. Kaminski, S. F. Hanna, and R. P. Lucht, *Phys. Rev. A* **64**, 063816 (2001).